Available online at www.sciencedirect.com
SCIENCE DIRECT®
Computers & Fluids 35 (2006) 74–102
computers & fluids
www.elsevier.com/locate/compfluid

An investigation of pulsating turbulent open channel flow by large eddy simulation

Li-Yong Zou, Nan-Sheng Liu, Xi-Yun Lu *

Department of Modern Mechanics, University of Science and Technology of China, Hefei, Anhui 230026, PR China

Received 1 October 2003; received in revised form 15 April 2004; accepted 9 October 2004
Available online 21 December 2004

Abstract

Pulsating turbulent open channel flow is investigated by use of large eddy simulation (LES) technique coupled with a dynamic subgrid-scale (SGS) model for turbulent SGS stress. The three-dimensional filtered Navier–Stokes equation is numerically solved by a fractional-step method. The objective of this study is to deal with the behaviors of pulsating turbulent open channel flow, in particular turbulence characteristics in the free surface-influenced layer, and to examine the reliability of the LES approach for predicting the pulsating turbulent flow with a free surface. In this study, the frequency of driving pressure gradient ranges low, medium and high value. The mean and phase-averaged statistical turbulence quantities, the resolved turbulent kinetic energy and Reynolds stresses budgets, and the flow structures are obtained and analyzed. With the increase of the driving frequency, the depth of the surface-influenced layer increases and the turbulent Stokes length near the bottom wall decreases. Different turbulence characteristics between the accelerating and decelerating phases are interpreted comprehensively. Turbulence intensities reveal that turbulent flow has a strong anisotropy in the free surface-influenced layer, in particular in the decelerating phases during the pulsating cycle. The budget terms of the resolved turbulent kinetic energy, the vertical and spanwise Reynolds stresses in the free surface region are analyzed. The flow structures clearly exhibit that bursting processes near the bottom wall are ejected toward the surface and the most surface renewal events are closely correlated with the bursting processes. These processes are strengthened during the decelerating period since strong turbulence intensities are generated.

* Corresponding author. Tel.: +86 551 360 3223; fax: +86 551 360 6459.
E-mail address: xlu@ustc.edu.cn (X.-Y. Lu).

0045-7930/$ - see front matter © 2004 Elsevier Ltd. All rights reserved.
doi:10.1016/j.compfluid.2004.10.001

1. Introduction

Understanding and prediction of the interaction of turbulence with a free surface are of great interest in applications and fundamentals. The turbulence structure near the free surface is a key factor to reveal more fundamental knowledge of the interaction of turbulence with the surface. On the other hand, inherent unsteadiness of driving condition, e.g., time-varying pressure gradient, characterizes a variety of time-dependent turbulent flows. To the best of our knowledge, however, pulsating turbulent open channel flow driven by an oscillating pressure gradient is a typical case for unsteady turbulent flow with a free surface and has never been examined. Here, the relevant work on the turbulent open channel flows and unsteady turbulent flows driven by time-varying external forces is briefly reviewed.

Usually, a natural and convenient way to investigate the free surface turbulent flow is by use of a fully developed turbulent open channel flow, where the turbulence that arrives at the free surface is produced principally at the bottom solid wall. Based on experimental visualization [1–4], the most surface renewal events are due to bursting processes near the solid boundary, and verified that large-scale, energy-containing eddies are primarily responsible for surface renewal. Further, some typical experiments [5–7] have found the existence of so-called surface renewal patches at the free surface, in particular, confirmed that a large fraction of surface renewal events originate from the buffer region of the boundary layer and are closely correlated with the boundary layer bursts. A relatively simple scenario emerges from these experiments; low-speed fluid is ejected toward the surface from the bottom wall, the fluid rises to the surface to form a surface renewal patch, and a downdraft develops after the interaction.

Although those experiments have demonstrated much about the processes involved in turbulent surface renewal, however, undergone considerable difficulty in making accurate velocity measurement very near the free surface. To some extent, an accurate numerical simulation can be employed to study this problem, allowing precise determination of the velocity field very close to the free surface. As well known, direct numerical simulation (DNS) approach can be used to calculate and analyze the behaviors of turbulence structure near the free surface. Some typical DNS calculations [8–13] have been carried out to investigate turbulence structures near the free surface in an open channel flow with a zero-shear interface. Tsai [11] studied numerically the interaction dynamics of the free surface with the coherent vortices in the underlying turbulent shear flow and the resulting free surface signatures, and found that coherent horseshoe vortical structures emerge from the random initial vorticity field. Nagaosa [12] studied the dynamics of well-organized tube-like coherent structures under a free surface and found the role of the vortex and surface interactions on the dynamics of turbulence under the free surface, particularly intercomponent energy transfer due to the pressure-strain effect. Handler et al. [13] investigated fully developed turbulence in the open channel, and revealed the wake-like structure of the patches at the free surface and the importance of the interaction of turbulent structures in free surface with scalar transport.

It is now well established that large eddy simulation (LES) technique, which solves only the large-scale components of turbulent flow and models the subgrid-scales (SGS) effects via SGS models, provides an effective tool to study some detailed features of turbulent flows. The SGS model is a key problem. A dynamic SGS model was proposed by Germano et al. [14] which overcame some shortcomings of the classical Smagorinsky model [15]. The dynamic model gained a

remarkable success in the past decade and it gave a new impetus to the development of new strategies for the LES [16–19]. On account of the improvements made by the SGS models, it becomes highly tempting to use the dynamic SGS model for studying turbulent flow [20,21].

To obtain reliable LES results for turbulent flow near a free surface, it is necessary to ensure that replacing DNS by LES will not produce significant deviation in the large scales of the turbulent flow field. Based on recent work [22,23], it is found that, since turbulence distortion is less severe near a free surface than near a solid wall, there is no doubt that the LES approach provides an accurate description of the large-scale dynamics in the surface-influenced region of an open-channel flow. Salvetti et al. [22] employed the LES technique to investigate decaying turbulence in an open channel using dynamic SGS models, and verified that the LES approach is able to reproduce the features of the decay process observed in the direct simulation and to handle the anisotropic nature of the flow. Calmet and Magnaudet [23] performed LES to deal with statistical characteristics of turbulence in the near surface region for a steady open channel flow at a high-Reynolds-number. They revealed that the correct dissipation profile close to the surface being recovered through the LES calculation, in which the small-scale processes are not resolved, confirms that near-surface dissipation is essentially governed by viscous effects affecting the large-scale motions. Meanwhile, the LES approach with dynamic SGS models has already been employed to study a fully developed turbulent open channel flow with scalar transfer [24]. It was confirmed that the LES results exhibited a very good quantitative agreement with known turbulent statistics and well-established correlations for the scalar transfer rate.

Although a variety of turbulent flows have been investigated by means of LES technique, very little work has been performed for unsteady turbulent flow and many aspects of wall turbulence in unsteady flows are still unknown. Lu et al. [25] performed the LES calculation for an oscillating flow past a circular cylinder. Hsu et al. [26] dealt with an oscillating turbulent flow over a flat plate and verified that the LES approach coupled with the dynamic SGS model is suited to tackle unsteady problem. Then, Scotti and Piomelli [27] investigated pulsating turbulent channel flow driven by oscillating pressure gradient and demonstrated that the LES can reasonably predict statistical unsteady turbulence behavior. Recently, Wang and Lu [28] further investigated oscillating turbulent channel flow with heat transfer by use of LES approach. Meanwhile, some typical work based on DNS [29–32] has been performed to investigate turbulence characteristics and structures in unsteady turbulent flows, and in particular in oscillating or pulsating flows. However, the lack of a deep knowledge of unsteady turbulence still exists and is largely due to the difficulties encountered when making accurate measurements of turbulence characteristics in rapidly varying flows and in tackling the problem by analytical means.

In this study, LES approach is used to calculate pulsating turbulent open channel flow driven by an oscillating pressure gradient. The motivation is to investigate the behaviors of the pulsating turbulent open channel flow, in particular in the free surface-influenced layer, and to examine the reliability of the LES approach for predicting the pulsating turbulent flow. The three-dimensional resolved incompressible Navier–Stokes equations are solved by the fractional-step method proposed by Verzicco and Orlandi [33]. Dynamic SGS model for SGS turbulent stress is employed to close the equations.

This paper is organized as follows. The mathematical formulation and the dynamic SGS model for modeling turbulent stresses are described in Section 2. The numerical method and its validation are given in Section 3. In Section 4, the mean and phase-averaged turbulence statistical

quantities, the resolved turbulent kinetic energy and Reynolds stresses budgets, and the flow structures are discussed. Finally, concluding remarks are summarized in Section 5.

2. Mathematical formulations

To investigate pulsating turbulent open channel flow with in the absence of significant surface deformations or buoyancy effects near the free surface, as schematically shown in Fig. 1, the three-dimensional filtered incompressible Navier–Stokes equations are solved. To non-dimensionalize the Navier–Stokes equations, the mean wall friction velocity u_τ, defined in the following, is used as the velocity scale, and the channel depth δ as the length scale. Then, the non-dimensional governing equations are given as

$$\frac{\partial \bar{u}_i}{\partial x_i} = 0, \tag{1}$$

$$\frac{\partial \bar{u}_i}{\partial t} + \frac{\partial}{\partial x_j}(\bar{u}_i \bar{u}_j) = -\frac{\partial \bar{p}}{\partial x_i} + \frac{1}{Re_\tau}\frac{\partial^2 \bar{u}_i}{\partial x_j \partial x_j} - \frac{\partial \tau_{ij}}{\partial x_j} + P_g \delta_{i1}, \tag{2}$$

where $\tau_{ij} = R_{ij} - \delta_{ij}R_{kk}/3$, $R_{ij} = \overline{u_i u_j} - \bar{u}_i \bar{u}_j$, overbar "–" represents the resolved variable. The Reynolds number Re_τ is defined as $Re_\tau = u_\tau \delta/\nu$ with ν being the kinematic viscosity. $\bar{u}_i$ is the resolved velocity. In this study, the resolved velocity $\bar{u}_i$ ($i = 1, 2, 3$), for writing convenience, is represented as u, v and w in the streamwise (x), spanwise (y) and vertical (z) directions, respectively. $\bar{p}$ is the resolved modified pressure, which contains a term $R_{kk}/3$. $P_g\delta_{i1}$ denotes an external pressure gradient along the streamwise direction, and the pressure gradient P_g represents

$$P_g = 1 + A_P \cos(\omega_P t), \tag{3}$$

where $\omega_P = 2\pi/t_P$, and A_P, ω_P and t_P represent the amplitude, frequency and period of the oscillating pressure gradient, respectively. Then, as used by Scotti and Piomelli [27], the friction velocity u_τ is defined based on the mean part of the pressure gradient in Eq. (3).

In Eq. (2), τ_{ij} represents SGS turbulent stress, which needs to be modeled by SGS model, and is written as,

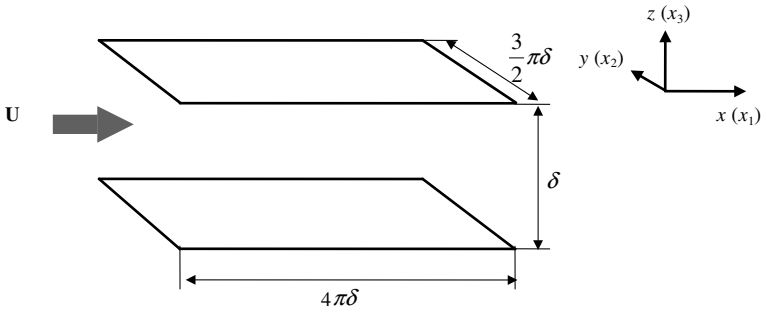

Fig. 1. Sketch of pulsating turbulent open channel flow.

$$\tau_{ij} = -2C\overline{\Delta}^2|\overline{S}|\overline{S}_{ij}, \tag{4}$$

where $\overline{S}_{ij} = (\partial\bar{u}_i/\partial x_j + \partial\bar{u}_j/\partial x_i)/2$, $|\overline{S}| = [2\overline{S}_{ij}\overline{S}_{ij}]^{\frac{1}{2}}$, and $\overline{\Delta}$ is the filter width.

Here, the model coefficient of C in Eq. (4) is obtained by use of the approach proposed by Germano et al. [14]. After introducing a test filtering with a filter width $\widehat{\overline{\Delta}}$ to Eqs. (1) and (2), the coefficients C can be dynamically determined as

$$C = -\frac{1}{\overline{\Delta}^2}\frac{\langle L_{ij}M_{ij}\rangle_S}{\langle M_{ij}M_{ij}\rangle_S}, \tag{5}$$

where $M_{ij} = 2\alpha^2|\widehat{\overline{S}}|[\widehat{\overline{S}}_{ij} - \frac{1}{3}\widehat{\overline{S}}_{kk}\delta_{ij}] - \hat{m}_{ij}$, $m_{ij} = 2|\overline{S}|\left[\overline{S}_{ij} - \frac{1}{3}\overline{S}_{kk}\delta_{ij}\right]$, and $L_{ij} = \widehat{\bar{u}_i\bar{u}_j} - \hat{\bar{u}}_i\hat{\bar{u}}_j - \frac{1}{3}(\widehat{\bar{u}_k\bar{u}_k} - \hat{\bar{u}}_k\hat{\bar{u}}_k)\delta_{ij}$.

Here, $\alpha = \widehat{\overline{\Delta}}/\overline{\Delta}$ is chosen as $\sqrt{6}$ [34] in the present calculation, $\langle\cdot\rangle_S$ denotes some kind of spatial averaging to remove the calculation oscillation [14,15]. In the present calculation, the average is taken in the plane parallel to the bottom wall [23,24]. It is still needed to note that the validity of the dynamic SGS model to deal with unsteady turbulent flow has been established by performing detailed validation and verification in [26–28].

As shown in Fig. 1, no-slip and no-penetration velocity conditions are imposed at the bottom wall $z = 0$. The boundary conditions applied at $z = 1$ are those for a shear-free interface without deformation, i.e.,

$$\bar{w} = 0, \quad \frac{\partial\bar{u}}{\partial z} = \frac{\partial\bar{v}}{\partial z} = 0. \tag{6}$$

The flow field is assumed to be statistically homogeneous in the streamwise and spanwise directions. Thus, periodic boundary conditions are employed in both the directions.

3. Numerical methods

To perform LES calculation, a fractional-step method developed by Verzicco and Orlandi [33] is used to solve Eqs. (1) and (2). Spatial derivatives are discretized by a second order central difference. Time advancement is carried out by the semi-implicit scheme using the Crank–Nicholson scheme for the viscous terms and the three-stage Runge–Kutta scheme for the convective terms. The low-storage Runge–Kutta methods have the additional advantage that the minimum amount of computer run-time memory is realized. The discretized formulation was described in detail in [33].

The size of computational domain is $4\pi\delta \times 3\pi\delta/2 \times \delta$ with the corresponding grid number $97 \times 97 \times 97$ in the streamwise, spanwise and vertical directions, respectively. The domain size is chosen such that two-point correlations in both the streamwise and spanwise directions are negligibly small. The grid independence of the present calculation has been ensured for every simulation. The grid is uniform along both the streamwise and spanwise directions. In the vertical direction, to increase the grid resolution near the free surface and the bottom wall, respectively, the mesh is stretched following the transformation, i.e.,

$$z_k = \frac{1}{2} + \frac{1}{2a}\tanh[\zeta_k\tanh^{-1}(a)], \tag{7}$$

where $\zeta_k = -1 + 2(k-1)/(N-1)$ and $k = 1,\ldots,N$. The value of a is selected so that the grid distribution in the z-direction is sufficient to resolve the viscous sublayer near the bottom wall and at the free surface [21,24].

To validate quantitatively the present calculation, a fully developed turbulent open channel flow is calculated at $Re_\tau = 180$, which has been investigated numerically and experimentally [8,13]. Fig. 2 shows the mean streamwise velocity versus z^+, where z^+ is the vertical distance from the bottom wall normalized by the friction velocity and is defined as $z^+ = zu_\tau/\nu$. Based on the previous work [9–13], the velocity statistics near the no-slip boundary are not affected by the existence of a free surface. Thus, there exists a buffer layer followed by a standard logarithmic region in the mean velocity profile, which is closely similar to that of fully developed turbulent channel flow. However, there is a slight deviation from the classic logarithmic region in the wall law for $z^+ > 100$ which must be assumed to be due to the presence of the free surface. Furthermore, some typical experimental data [8] and DNS result [13] are also plotted in Fig. 2; our calculated results are in good agreement with those results.

The turbulence intensity profiles, based on the root-mean-square values of the streamwise, spanwise and vertical velocity fluctuations (i.e., u_{rms}, v_{rms} and w_{rms}), are shown in Fig. 3. The turbulence intensities present a strong anisotropy near the free surface and exhibit characteristics near the bottom wall being in agreement with two-walled channel flow [20,21]. Meanwhile, it is seen that our calculated result agrees well with the experimental data [8] and DNS result [13].

Moreover, extensive validations have been performed in our previous work for turbulent open channel flow with heat transfer [24], unsteady turbulent channel flow with heat transfer [28,35], and turbulent flow with passive scalar transfer [20,21]. Thus, it can be confirmed that our calculation is reliable for the prediction of the turbulent flows.

4. Results and discussion

Here, some typical calculations have been performed for different oscillating frequencies at $Re_\tau = 180$. The pulsating turbulent flow with the mean and the oscillating parts is driven by the

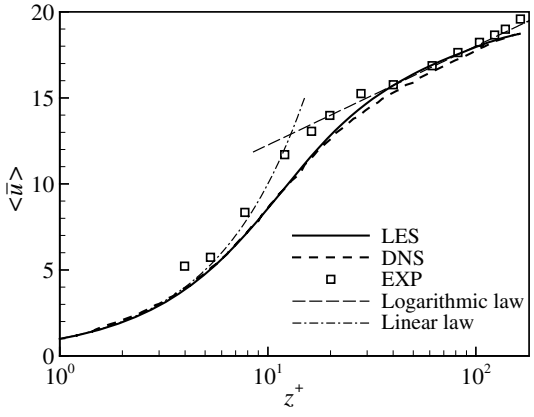

Fig. 2. Profile of the mean streamwise velocity for fully developed turbulent open channel flow and comparison with experimental data [8] and computational result [13].

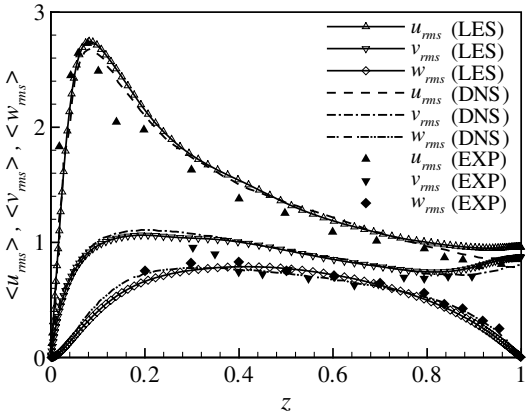

Fig. 3. Profiles of the root-mean-square velocity and comparison with experimental data [8] and DNS result [13].

pressure gradient in Eq. (3). The amplitude (A_P) and the frequency (ω_P) of oscillating pressure gradient are listed in Table 1, which were investigated correspondingly for turbulent two-walled channel flow [27,28]. Three cases listed in Table 1 correspond to low, medium and high frequency with the ratio between the oscillating and mean velocity at the free surface approximately 0.7.

To elucidate the pulsating turbulent open channel flow driven by the oscillating pressure gradient, the mean and phase-averaged statistical turbulent quantities are analyzed. To remove initial effect, the mean and phase-averaged statistical quantities are calculated in several pulsating periods after the flow reaches statistically unsteady state. The mean quantity is calculated by taking an average in the whole time and in the plane parallel to the bottom wall and denoted by $\langle \cdot \rangle_T$, and the phase-averaged quantity is obtained by averaging in the plane parallel to the wall at the same phase and represented by $\langle \cdot \rangle_P$.

4.1. Pulsating turbulent flow characteristics

Fig. 4 shows the profiles of mean streamwise velocity (i.e., $\langle \bar{u} \rangle_T$) for three driving frequencies. It is found that the results collapse on a buffer layer followed by a logarithmic layer for all frequencies examined, which are similar to that of a fully developed turbulent open channel flow driven by constant pressure gradient, as shown in Fig. 2. This behavior is consistent with the results obtained numerically [27,28] and experimentally [36] for pulsating turbulent channel flow, where it was verified that the mean streamwise velocity did not show any significant change as the driving frequency varied in the regime considered in this study.

Table 1
The amplitude (A_P) and frequency (ω_P) of the pulsating pressure gradient

	ω_P	A_P
Low frequency	1.0	14.3
Medium frequency	3.5	50
High frequency	14.0	200

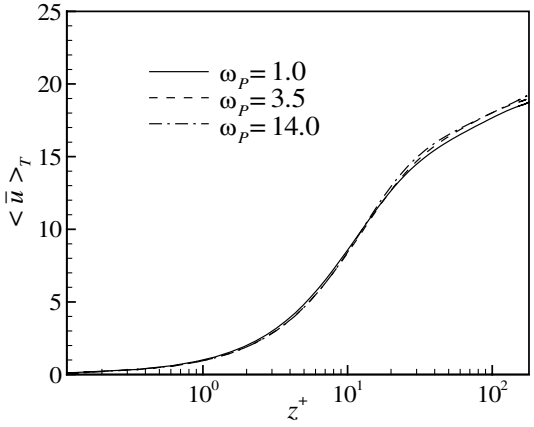

Fig. 4. Profiles of the mean streamwise velocity for different frequencies.

To deal with the variation of velocity during one cycle, Fig. 5 shows the phase-averaged streamwise velocity (i.e., $\langle \bar{u} \rangle_P$) profiles for $\omega_P = 1$ at several phases. Based on the velocity profiles near the free surface region, it can be reasonably identified that the accelerating phase is from $t/t_P = 6/8$ through 0/8 (or 8/8) to 2/8 approximately, and the decelerating phase from $t/t_P = 2/8$ to 6/8. Following the velocity profiles in the vicinity of the wall, a layer that obeys the semi-logarithmic law exists above the viscous sublayer. It is noted that the semi-logarithmic law regions in the accelerating phase are narrower and closer to the wall (e.g., $t/t_P = 0/8$, 1/8), while those in the decelerating phase are broader and farther away from the wall (e.g., $t/t_P = 3/8$, 4/8). The difference in turbulence characteristics between the accelerating and decelerating phases is closely related to turbulence production and turbulence anisotropy near the free surface and will be analyzed in the following based on the resolved turbulent kinetic energy budget.

The phase-averaged root-mean-square (rms) values (or turbulence intensities) of the velocity fluctuations in the streamwise, spanwise and vertical directions at $\omega_P = 1$ are shown in Fig. 6.

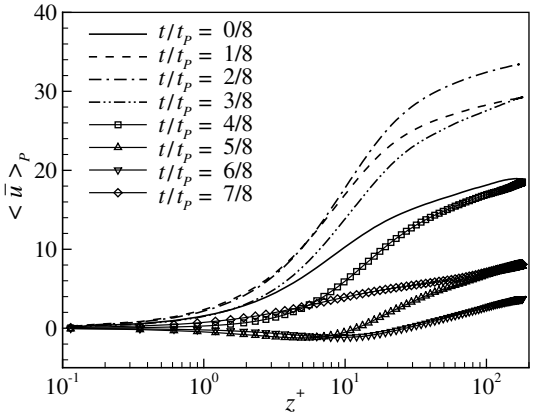

Fig. 5. Profiles of the phase-averaged streamwise velocity at $\omega_P = 1$.

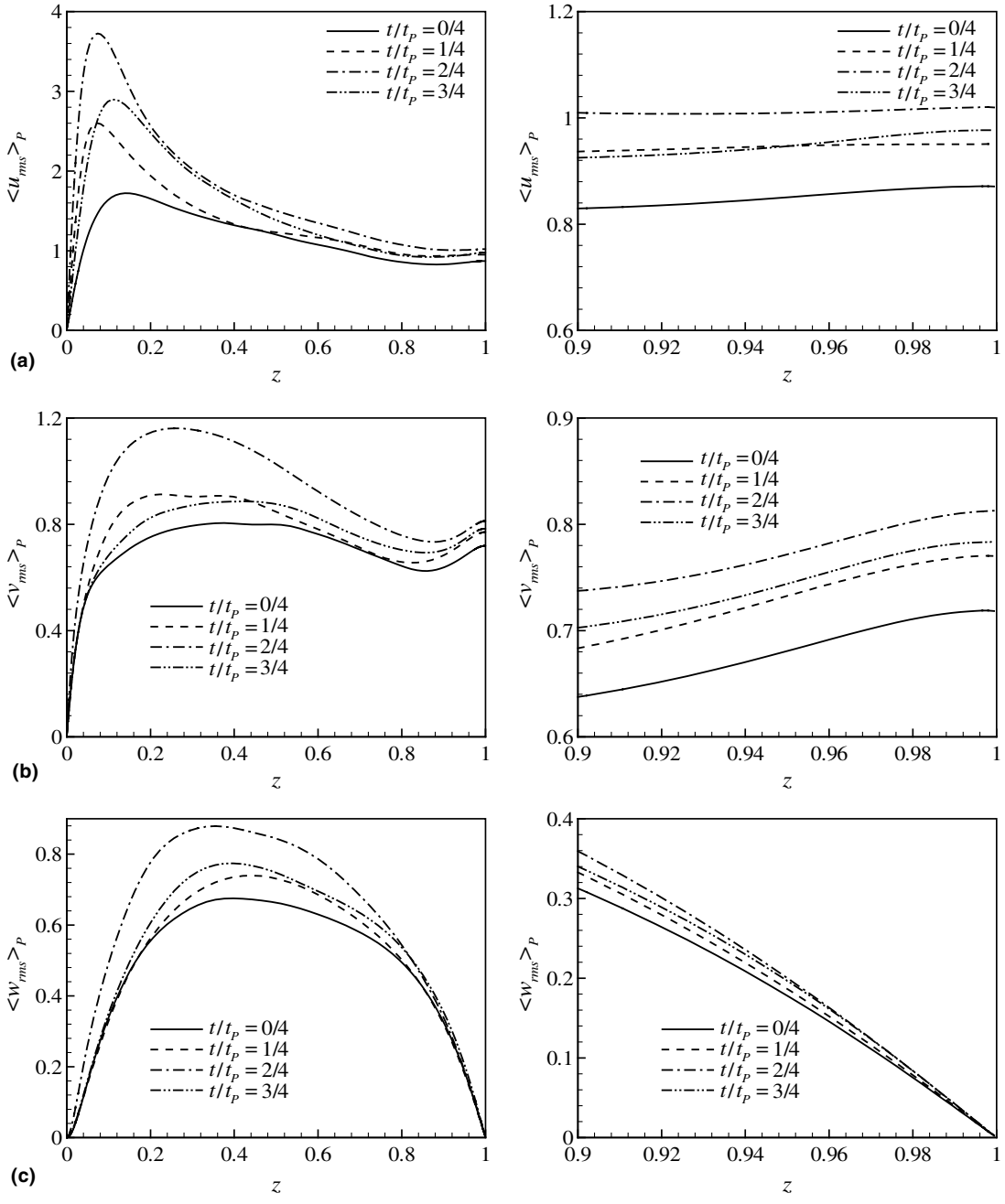

Fig. 6. Distributions of the phase-averaged velocity fluctuations over the channel (left column) and near the free surface (right column) for $\omega_P = 1$: (a) $\langle u_{\mathrm{rms}} \rangle_P$; (b) $\langle v_{\mathrm{rms}} \rangle_P$; (c) $\langle w_{\mathrm{rms}} \rangle_P$.

The distributions of turbulence intensities in the decelerating phase (e.g., $t/t_P = 2/4$) are higher than those in the accelerating phase (e.g., at $t/t_P = 0/4$). This behavior means that the velocity

fluctuations are mainly generated during the deceleration and suppressed during the acceleration, which was verified experimentally and numerically [26,28,37].

Further, turbulence characteristics in the free surface-influenced layer, which have never been dealt with for pulsating turbulent flow in an open-channel, are discussed. The depth of the surface-influenced region can be qualitatively denoted by the position where the free surface begins to damp the vertical velocity fluctuation [23], correspondingly, to enhance the spanwise velocity fluctuation because the turbulence energy is mainly transferred from the vertical to spanwise direction near the free surface due to the organized structure represented as "dipole vorticity", where two vortices are aligned along the streamwise direction [24]. From Fig. 6b, the depth of the surface-influenced region (z_S) can be determined by the distance from the free surface to the location of minimum of the spanwise velocity fluctuation (i.e., $\langle v_{\mathrm{rms}}\rangle_P$) and is listed in Table 2 for $\langle z_S\rangle_P$ at several phases. Meanwhile, to analyze conveniently the relation of the surface-influenced layer with the turbulence intensities in the near wall region, the distance from the wall to the location of maximum of the streamwise velocity fluctuation (i.e., z_W) is obtained in Table 2 for $\langle z_W\rangle_P$.

During the decelerating phase (e.g., $t/t_P = 2/4$), both $\langle z_S\rangle_P$ and $\langle z_W\rangle_P$ become smaller obviously. As indicated by Calmet and Magnaudet [23], the anisotropy of the turbulence entering the surface region directly influences the turbulence behaviors near the free surface and is closely related to the exchange between the vertical velocity fluctuation component and the tangential ones. The relative turbulence intensities at z_S (corresponding to the bottom boundary of free surface-influenced layer), i.e., u_{rms}^2/k, v_{rms}^2/k and w_{rms}^2/k with k denoting the phase-averaged turbulent kinetic energy, are given in Table 2. It is noted that stronger anisotropy of the near-surface turbulence during the decelerating phase appears. Correspondingly, during the accelerating phase (e.g., $t/t_P = 0/4$), both $\langle z_S\rangle_P$ and $\langle z_W\rangle_P$, compared to those at $t/t_P = 2/4$, gets larger, and the anisotropy of the turbulence entering the surface region becomes somewhat weaker.

Since the low-Reynolds number open channel flow is considered in this study, the bottom wall turbulent flow controls the turbulent structures almost entirely over the channel [23]. As shown in Fig. 6 for the distributions of turbulence intensities in the free surface-influenced region, it is evident that the pulsating effect has a significant influence on the entire flow. The values of turbulence intensities near the free surface in the decelerating phase (e.g., $t/t_P = 2/4$) are also higher than those in the accelerating phase (e.g., $t/t_P = 0/4$). This behavior is reasonably predicted since the most surface renewal events and large-scale, energy-containing eddies near the free surface are due to bursting processes near the bottom wall in the turbulent open channel flow [1–4].

Table 2
Distance from the wall to the location of maximum of the streamwise velocity fluctuation z_W, the depth of the surface-influenced region z_S, and the turbulence intensities with respect to the phase-averaged turbulent kinetic energy at z_S for $\omega_P = 1$

Phase (t/t_P)	$\langle z_W\rangle_P$	$\langle z_S\rangle_P$	$\langle u_{\mathrm{rms}}/k\rangle_P$	$\langle {v_{\mathrm{rms}}}^2/k\rangle_P$	$\langle {w_{\mathrm{rms}}}^2/k\rangle_P$
0/4	0.140	0.142	1.111	0.625	0.260
1/4	0.078	0.161	1.157	0.558	0.285
2/4	0.082	0.127	1.193	0.624	0.187
3/4	0.119	0.143	1.112	0.626	0.262

4.2. Effect of driving frequency on turbulent flow

To demonstrate the effect of driving frequency on turbulent flow characteristics, Figs. 7 and 8 show the phase-averaged velocity and its fluctuations in the streamwise, spanwise and vertical directions at $\omega_P = 3.5$ and 14, respectively. In order to classify the flows based on the driving frequency, a concept of turbulent Stokes length is introduced according to Scotti and Piomelli [27] and Tu and Ramaprian [38], which defines how far vorticity waves generated at the wall penetrate into the flow. Assuming that the effect of turbulence can be captured, at least qualitatively, by a simple eddy viscosity ν_T, and drawing an analogy to the laminar Stokes problem, the effect of the oscillation on the flow is confined to a layer of thickness l_T, where $l_T = [2(\nu + \nu_T)/\omega_P]^{1/2}$ is a turbulent Stokes length obtained using the sum of the molecular and turbulent diffusivities [27,38]. To exhibit the influence of the driving frequency, as listed in Table 3, $\langle z_W \rangle_T$, which represents reasonably a global effect during one cycle and is qualitatively relevant to the turbulent Stokes length, decreases with the increase of ω_P.

When the frequency of oscillation is small (or the period of oscillation is large), the turbulence has time to relax the local (in time) equilibrium [39] and the pulsating effect has a significant influence on the entire flow, as shown in Figs. 5 and 6 for $\omega_P = 1$. At high frequency, the penetration length is similar to that for laminar flow. The pulsating effect has somewhat little influence on the

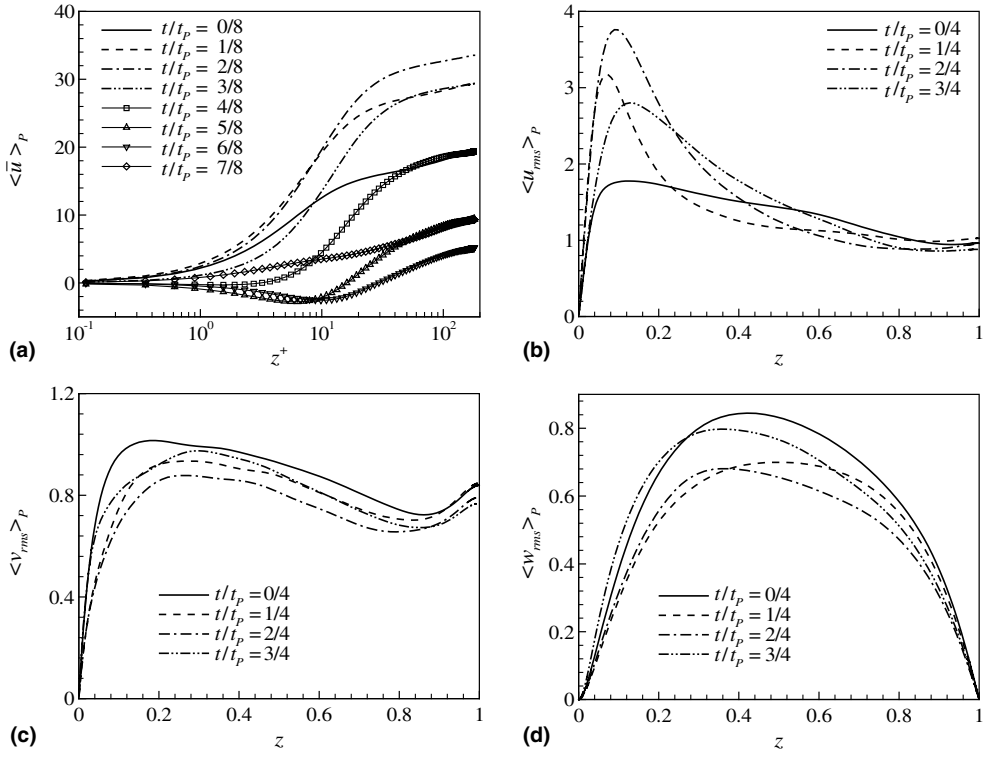

Fig. 7. Distributions of the phase-averaged velocity and velocity fluctuations at $\omega_P = 3.5$: (a) $\langle \bar{u} \rangle_P$; (b) $\langle u_{\mathrm{rms}} \rangle_P$; (c) $\langle v_{\mathrm{rms}} \rangle_P$; (d) $\langle w_{\mathrm{rms}} \rangle_P$.

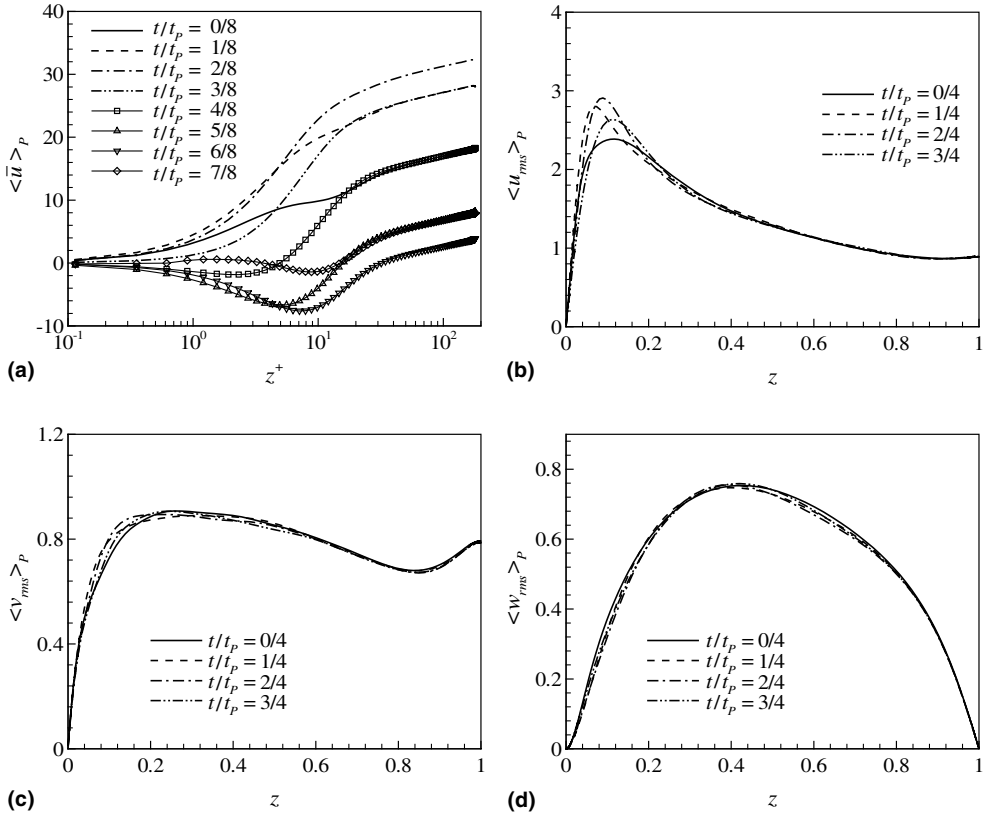

Fig. 8. Distributions of the phase-averaged velocity and velocity fluctuations at $\omega_P = 14$: (a) $\langle \bar{u} \rangle_P$; (b) $\langle u_{\mathrm{rms}} \rangle_P$; (c) $\langle v_{\mathrm{rms}} \rangle_P$; (d) $\langle w_{\mathrm{rms}} \rangle_P$.

Table 3
Distance from the wall to the location of maximum of the streamwise velocity fluctuation z_W and the depth of the surface-influenced region z_S for pulsating and non-pulsating cases

ω_P	$\langle z_W \rangle_T$	$\langle z_S \rangle_T$
1	0.105	0.143
3.5	0.101	0.151
14	0.095	0.158
Non-pulsating	0.089	0.178

flow. Thus, as shown in Fig. 8a for $\omega_P = 14$, the velocity profile in the outer region remains essentially unaltered and a logarithmic layer with the usual slope is illustrated, which is shifted upwards and downwards by the modulation of the outer region velocity, i.e., the profiles in the logarithmic region at different phases are parallel each other approximately. At medium frequency, as shown in Fig. 7 for $\omega_P = 3.5$, compared to low frequency in Fig. 6, the distributions of the spanwise and vertical intensities in the decelerating phase (e.g., $t/t_P = 2/4$) are obviously lower than those in the accelerating phase (e.g., $t/t_P = 0/4$). The behavior is closely related to the turbulent kinetic energy

transfer between the vertical and horizontal directions at medium frequency and is confirmed numerically for oscillating turbulent boundary flow [26,29].

The depth of the surface-influenced layer may have a relationship with the turbulent Stokes length in the open channel flow, which needs to be verified further, since eruption process of fluid from the bottom wall region usually retains their coherence in the sequence of convecting toward the free surface [5–7]. To exhibit the global behavior of the driving frequency, as shown in Table 3, $\langle z_S \rangle_T$ increases with the increase of ω_P. Meanwhile, as shown in Fig. 3, the depth of the surface-influenced layer for non-pulsating case can be determined as $z_S = 0.178$ approximately, which is higher than those for pulsating cases. This feature reasonably represents that the pulsating effect enhances the influence of turbulent structures in the free surface region with respect to the non-pulsating case.

4.3. Resolved turbulent kinetic energy and Reynolds stress budgets

As shown in Fig. 6, the turbulence intensities have a strong anisotropy near the free boundary, in particular during the decelerating phases. To explore the mechanism of the anisotropic behavior, the effect of the pressure-strain on the energy transfer and anisotropy character near the free surface is investigated, and the phase-averaged pressure-strain tensors are defined as

$$\langle \phi_{ij} \rangle_P = \left\langle p' \left(\frac{\partial u_i'}{\partial x_j} + \frac{\partial u_j'}{\partial x_i} \right) \right\rangle_P, \tag{8}$$

where p' and u_i' represent the resolved pressure and velocity fluctuations, respectively. The trace of the tensor (i.e., $\langle \phi_{ij} \rangle_P$) is always zero because of the incompressible constraint.

The distributions of the phase-averaged pressure-strain terms are shown in Fig. 9a–c in the streamwise, spanwise and vertical directions, respectively. In the near wall region, the role of the pressure-strain is similar to the oscillating turbulent wall bounded flow, the pressure-strain term in the streamwise direction ($\langle \phi_{11} \rangle_P$) mainly contributes to the turbulent energy redistribution [40], because it drains the turbulent energy from the streamwise turbulence fluctuation to the spanwise and vertical components at different phases. Here, we mainly concern the behavior of the pressure-strain terms in the free surface-influenced region. The value of the pressure-strain in the streamwise direction ($\langle \phi_{11} \rangle_P$) near the free surface is smaller than that of the pressure-strain in the spanwise direction ($\langle \phi_{22} \rangle_P$) at the same phase, while the values of $\langle \phi_{22} \rangle_P$ increase in the vicinity of the free surface and remain positive for $z > 0.96$ approximately. The distributions of the pressure-strain in the vertical direction ($\langle \phi_{33} \rangle_P$) decrease near the free surface and their signs change from positive to negative at $z = 0.9$ approximately, which lies in the free surface-influenced layer since $\langle z_S \rangle_T = 0.143$ as listed in Table 3. It is suggested that the turbulence energy in the vertical direction is mainly transferred into the spanwise direction through the pressure-strain effect and this process occurs in the free surface-influenced region.

As shown in Figs. 6 and 9, it is needed to discuss the relation between the pressure-strain and turbulence intensity, in particular near the free surface, at different phases. Near the free surface, $\langle \phi_{11} \rangle_P$ and $\langle \phi_{22} \rangle_P$ reach higher positive values and $\langle \phi_{33} \rangle_P$ has lower negative value during the decelerating period (e.g., $t/t_P = 2/4$), compared to those during the accelerating period (e.g., $t/t_P = 0/4$). Thus, as shown in Fig. 6, the corresponding turbulence intensities in the spanwise and streamwise direction increase obviously near the free surface at $t/t_P = 2/4$.

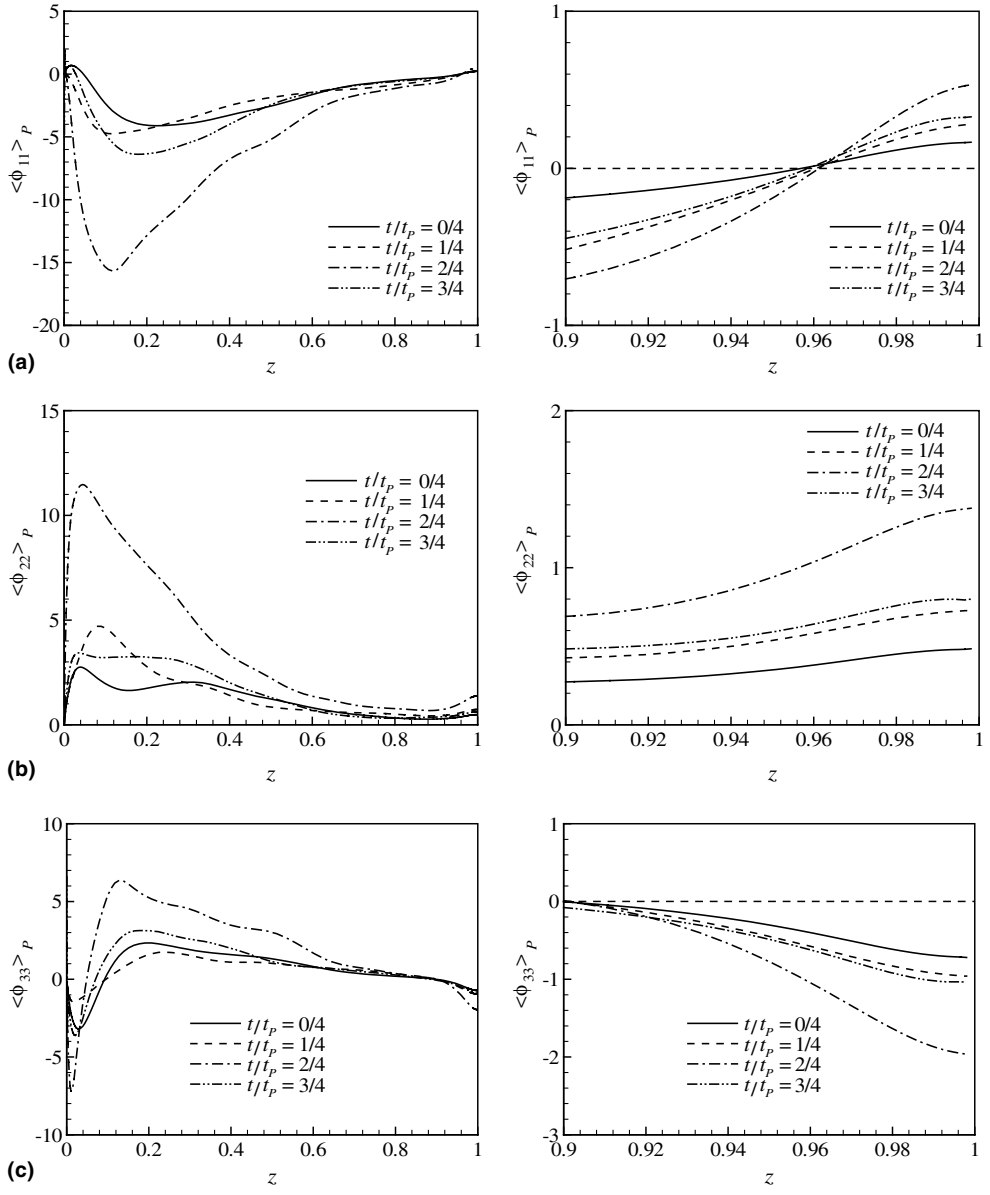

Fig. 9. Distributions of the phase-averaged pressure-strain terms over the channel (left column) and near the free surface (right column) for $\omega_P = 1$: (a) $\langle\phi_{11}\rangle_P$; (b) $\langle\phi_{22}\rangle_P$; (c) $\langle\phi_{33}\rangle_P$.

To analyze the mechanism of strong anisotropy and turbulent energy transfer among three directions near the free surface, the turbulent kinetic energy and Reynolds stresses budgets are further discussed. The resolved turbulent kinetic energy (TKE) budget terms based on the phase-averaged equation, referred to Eq. (A.1) in Appendix A, are shown in Fig. 10 for $\omega_P = 1$. By view of the distributions of the energy production (PR) and viscous dissipation (DS) for several phases,

it is noted that turbulence is mainly produced near the bottom wall. The turbulence kinetic energy balances between PR and DS reveal that the turbulence production in the region $0.5 < z < 1$ is at least one order of magnitude less than its peak value near the bottom wall. The behavior is certainly in accordance with the experiments [2,3], which have shown that surface renewal events have their origin principally in the region of the bottom wall. Based on the profiles of the budget terms in the streamwise Reynolds stress (i.e., $\langle u_1' u_1' \rangle$) transport equation (not shown here), the behavior for the balance between the energy production and viscous dissipation is similar to that depicted in Fig. 10. In the near wall region, the budget balance mainly holds for the terms of PR, DS, TD and VD, and the term of PD is small for several phases. Near the free surface, as indicated early, the production PR becomes very small and other terms including DS, TD and VD adjust accordingly. By comparing with the profiles at different phases, it is reasonably found that the magnitudes of these budget terms at the decelerating phase $t/t_P = 2/4$ (Fig. 10c) are higher than those at the accelerating phase $t/t_P = 0/4$ (Fig. 10a). This behavior is consistent with the turbulence intensity shown in Fig. 6.

In the free surface-influenced region, the dissipation becomes anisotropic due to the nature of the shear-free surface boundary conditions. Thus, the vertical fluctuation is preferentially dissipated, as shown in Fig. 6c, leading to an increase in stress anisotropy [13,24]. The budget terms in the resolved vertical Reynolds stress (i.e., $\langle u_3' u_3' \rangle$) transport equation, referred to Eq. (A.3) in

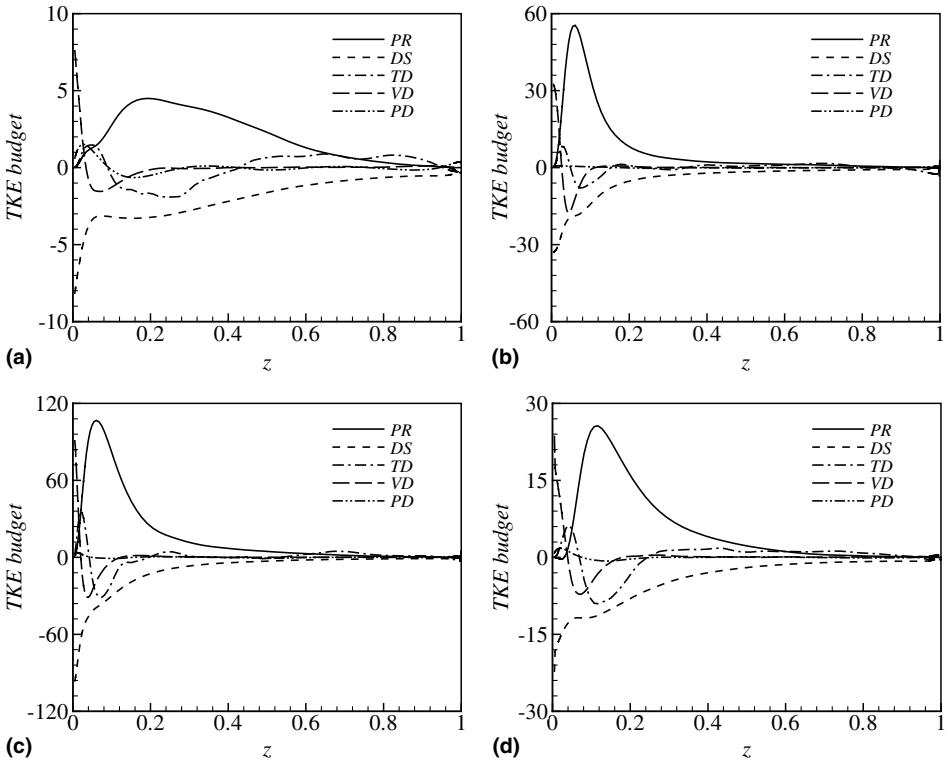

Fig. 10. Budget terms in the resolved turbulent kinetic energy equation for $\omega_P = 1$: (a) $t/t_P = 0/4$; (b) 1/4; (c) 2/4; (d) 3/4.

Appendix A, are shown in Figs. 11 and 12 for $\omega_P = 1$. In the near wall region $z < 0.1$, the budget is balanced mainly between PS and PD for several phases. In the region $0.1 < z < 0.9$, the budget terms of $\langle u_3' u_3' \rangle$, i.e., PS, PD, DS and TD terms, are mainly contributed to the budget balance and the term VD is small. Further, to understand the vertical fluctuation dissipation behavior near the free surface, Fig. 12 shows the profiles of the budget terms near the free surface, where $z_F^+ = (1 - z)u_\tau/\nu$. It is seen that the budget is balanced mainly between PD and PS in the free surface region ($z_F^+ < 8$) and the terms of DS, TD and VD are smaller there. The term TD contributes appreciably to the $\langle u_3' u_3' \rangle$ budget in the local region around $z_F^+ = 11$. This fact is mainly due to the zero production term for the $\langle u_3' u_3' \rangle$ budget and the blocking effect of the boundary condition of free surface. In the open channel flow, as a result of zero production for the vertical velocity fluctuation near the free surface, the dynamic processes related to the diffusion effect, including PD, TD and VD terms, play an important responsibility to transferring turbulent energy from the wall region towards the free surface, acting as the source term to the $\langle u_3' u_3' \rangle$ budget [23,41]. So, it is reasonably predicted that, in the free surface region, the whole diffusion terms, i.e., PD + TD + VD, are positive, indicating a net transport of the vertical turbulence fluctuation towards the free surface. The blocking effect of the free surface damps the vertical velocity fluctuation quickly to be zero as approaching the free surface, and the vertical turbulent kinetic energy is mainly transferred

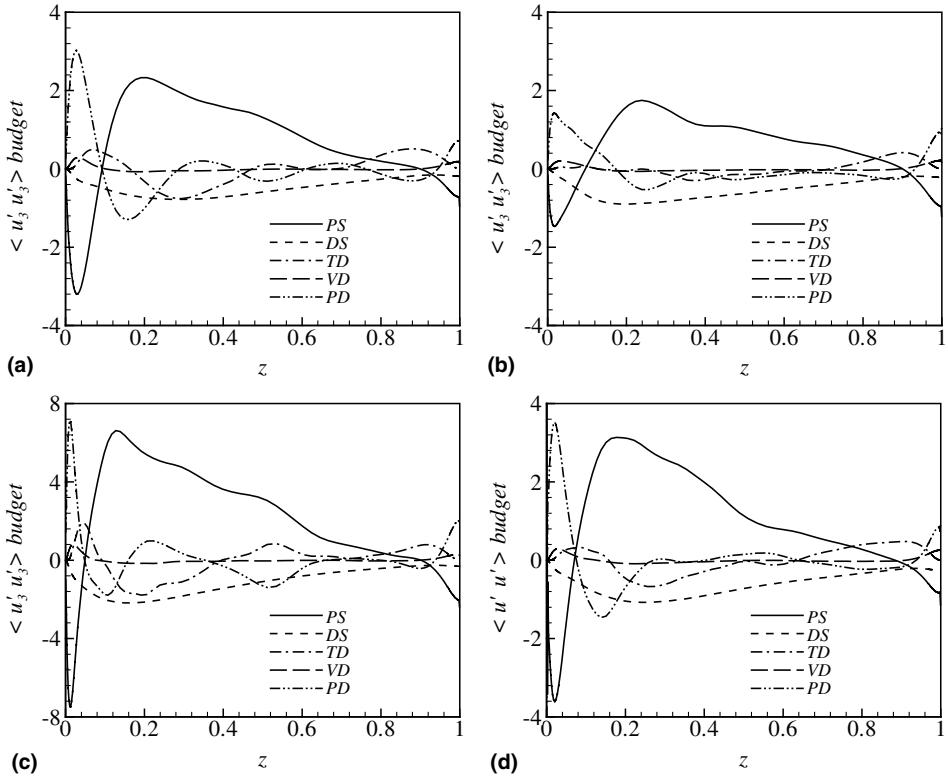

Fig. 11. Budget terms in the $\langle u_3' u_3' \rangle$ transport equation for $\omega_P = 1$: (a) $t/t_P = 0/4$; (b) 1/4; (c) 2/4; (d) 3/4.

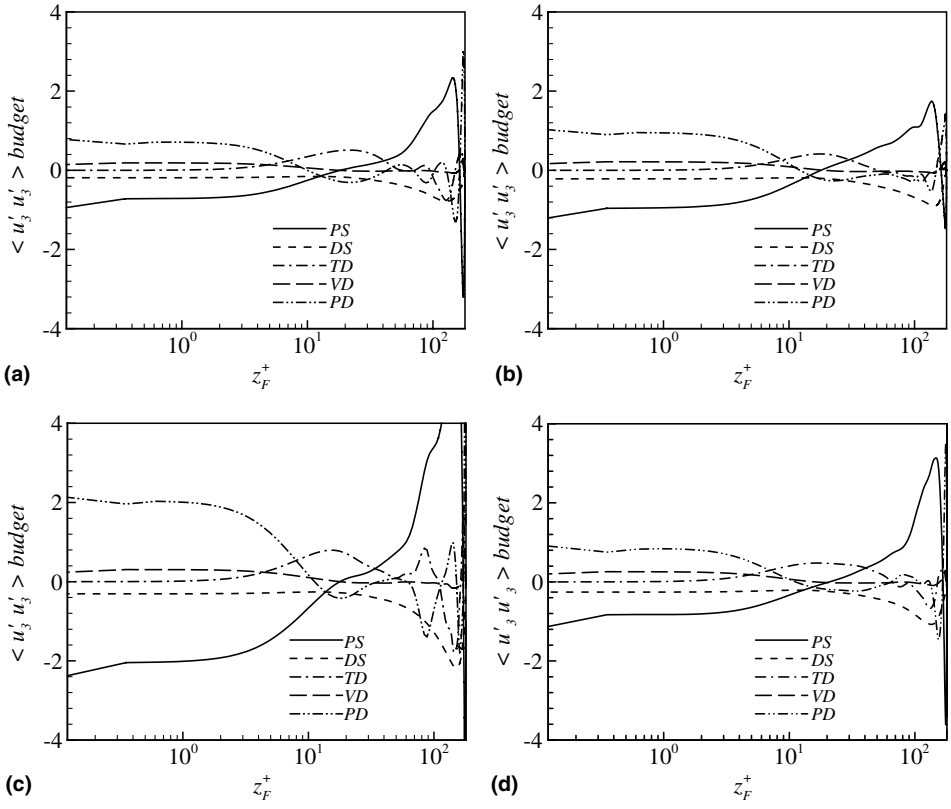

Fig. 12. Profiles of the budget terms in the $\langle u_3' u_3' \rangle$ transport equation near the free surface for $\omega_P = 1$: (a) $t/t_P = 0/4$; (b) 1/4; (c) 2/4; (d) 3/4.

to the spanwise component by PS term, increasing the local anisotropy [23]. Thus, PS term plays a dominant role to the $\langle u_3' u_3' \rangle$ budget in the surface-influenced region, accounting for the energy redistribution, as exhibited in Fig. 12. Meanwhile, as expected, the magnitudes of these budget terms at the decelerating phase $t/t_P = 2/4$ (Fig. 11c and Fig. 12c), compared to those at the accelerating phase $t/t_P = 0/4$ (Fig. 11a and Fig. 12a), exhibit higher level.

As discussed early, the turbulence energy in the vertical direction is mainly transferred into the spanwise direction through the pressure-strain effect. Thus, the budget terms in the resolved spanwise Reynolds stress (i.e., $\langle u_2' u_2' \rangle$) transport equation, referred to Eq. (A.2) in Appendix A, are further examined and shown in Figs. 13 and 14 for $\omega_P = 1$. As shown in Fig. 13, the budget balance mainly keeps between DS and VD in the viscous sublayer $z < 0.05$ (or around $z^+ < 9$) for several phases. The balance of $\langle u_2' u_2' \rangle$ budget in the region of $0.05 < z < 0.9$ is mainly due to the interaction between PS and DS terms with other terms TD and VD being smaller. As shown in Fig. 14, unlike the budget balance of $\langle u_3' u_3' \rangle$ in Fig. 12, all the terms of PS, DS, TD and VD contribute to the budget balance near the free surface, even the values of these terms near the free surface appear somewhat different but with the same order. The term PS is a main source term to the $\langle u_2' u_2' \rangle$ budget, responsible for the generation of the spanwise velocity fluctuation by the process of

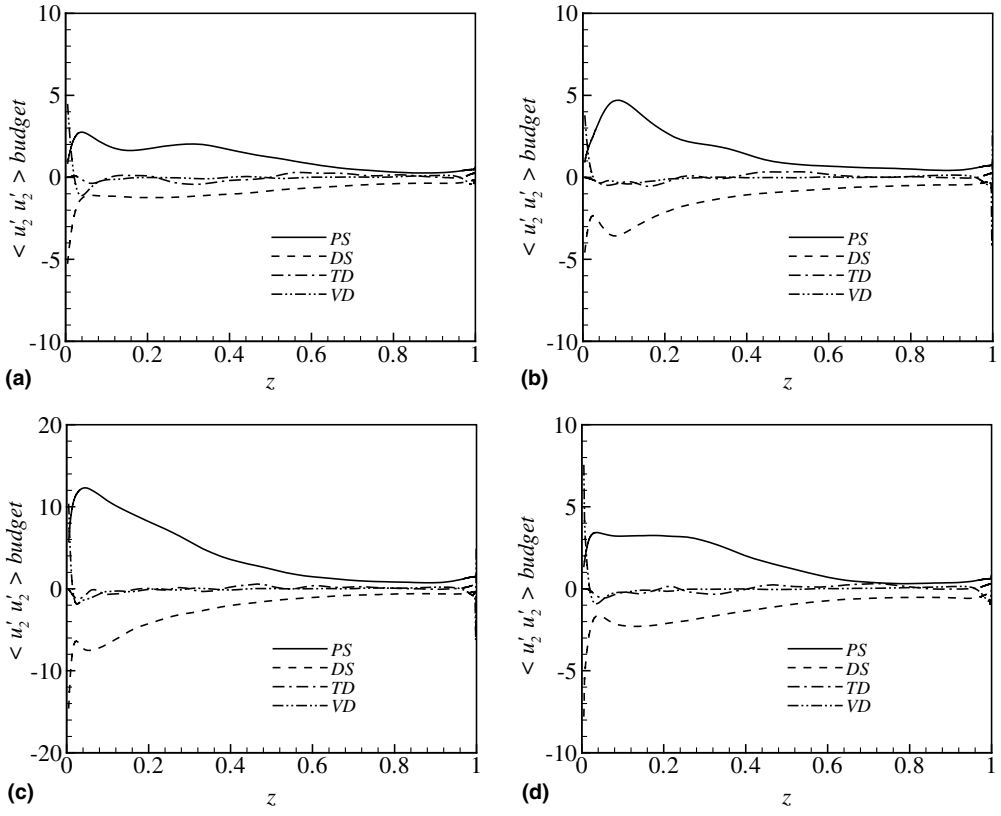

Fig. 13. Budget terms in the $\langle u_2' u_2' \rangle$ transport equation for $\omega_P = 1$: (a) $t/t_P = 0/4$; (b) 1/4; (c) 2/4; (d) 3/4.

energy transfer. In the close free surface region (i.e., $z_F^+ < 6$), the term TD is positive, transporting the spanwise turbulent kinetic energy towards the free surface. The term VD is a sink to the $\langle u_2' u_2' \rangle$ budget, indicating that the diffusion effect related to the fluid viscosity is to bring the turbulent energy away from the free surface. This fact is consistent with the distribution of v_{rms} in the surface region shown in Fig. 6b, and results in a negative value of the whole diffusion terms, corresponding to an inverse net transport of the spanwise turbulent kinetic energy with respect to that of the $\langle u_3' u_3' \rangle$ budget for $z_F^+ < 6$. However, the whole diffusion terms, i.e., PD + TD + VD, still contribute to transporting the spanwise velocity fluctuation towards the free surface for $z_F^+ > 6$. Similar to the trend of the $\langle u_3' u_3' \rangle$ budget, all the above budget terms exhibit higher level in the decelerating phase, compared to those in the accelerating phase.

4.4. Flow structures

It is evident that the turbulent structures at the free surface will vary spatially and temporally for pulsating turbulent open channel flow. Here, the structures of instantaneous velocity fluctuations are briefly discussed to support the time development of the turbulent quantities. Fig. 15

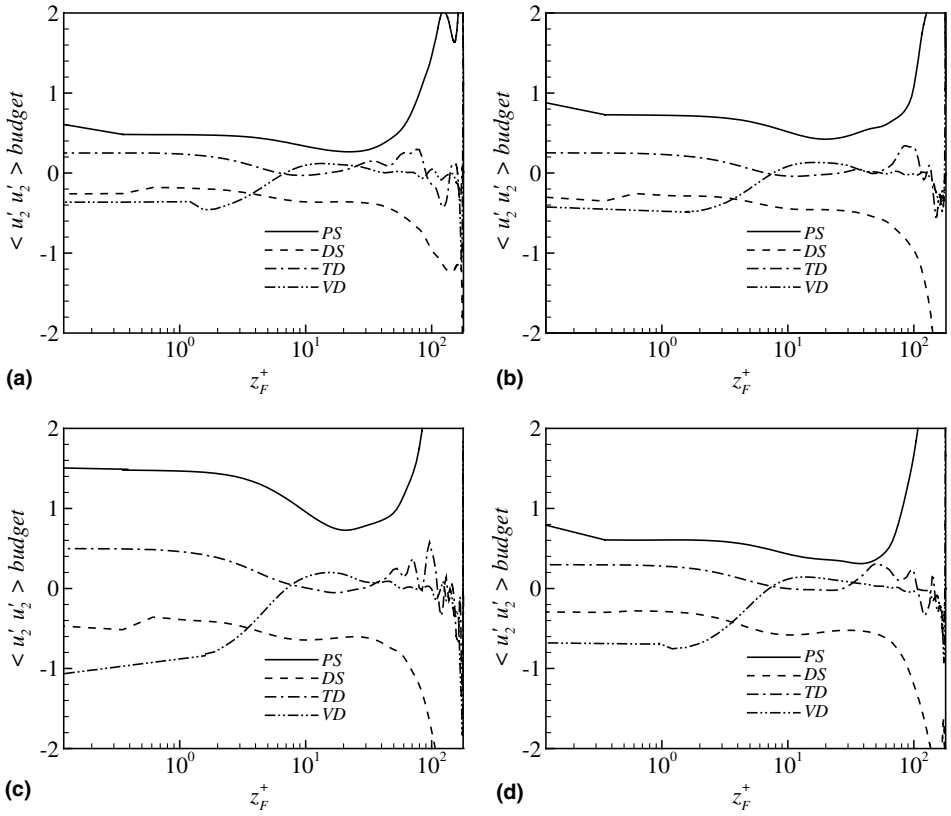

Fig. 14. Profiles of the budget terms in the $\langle u_2' u_2' \rangle$ transport equation near the free surface or $\omega_P = 1$: (a) $t/t_P = 0/4$; (b) 1/4; (c) 2/4; (d) 3/4.

shows the contours of instantaneous streamwise velocity fluctuation in the (x, y) plane at $z^+ = 6.5$ (i.e., near the bottom wall) for $\omega_P = 1$. The relevant discussion has been described numerically by Scotti and Piomelli [27] and experimentally Sarpkaya [42]. Further, we can analyze the structures based on the turbulent kinetic energy budget shown in Fig. 10. At $t/t_P = 0/4$ (Fig. 10a) and 3/4 (Fig. 10d), corresponding to the accelerating phase, the energy production (PR) is relatively restrained. The streaks are thus somewhat absent and the flow relaminarizes with little residual turbulent fluctuations at $t/t_P = 0/4$ (Fig. 15a), although relatively strong fluctuations with localized turbulent spots appear around $t/t_P = 3/4$ (Fig. 15d). During the decelerating phase, the energy production (PR) at $t/t_P = 1/4$ (Fig. 10b) and 2/4 (Fig. 10c) enhances turbulence significantly, in particular at $t/t_P = 2/4$. Thus, very long and smooth streaks develop and eventually fill the whole channel in Fig. 15b and c. The flow patterns exhibited in Fig. 15 are well consistent with the time development of the streamwise turbulent intensity given in Fig. 6a and are closely related to the balance among the turbulent kinetic energy budget terms shown in Fig. 10, in particular between the energy production (PR) and viscous dissipation (DS) in the near wall region.

The structures of the streamwise velocity fluctuation in the (x, y) plane at $z^+ = 173.5$, which lies in the free surface-influenced layer, are shown in Fig. 16. The structures are consistent with the

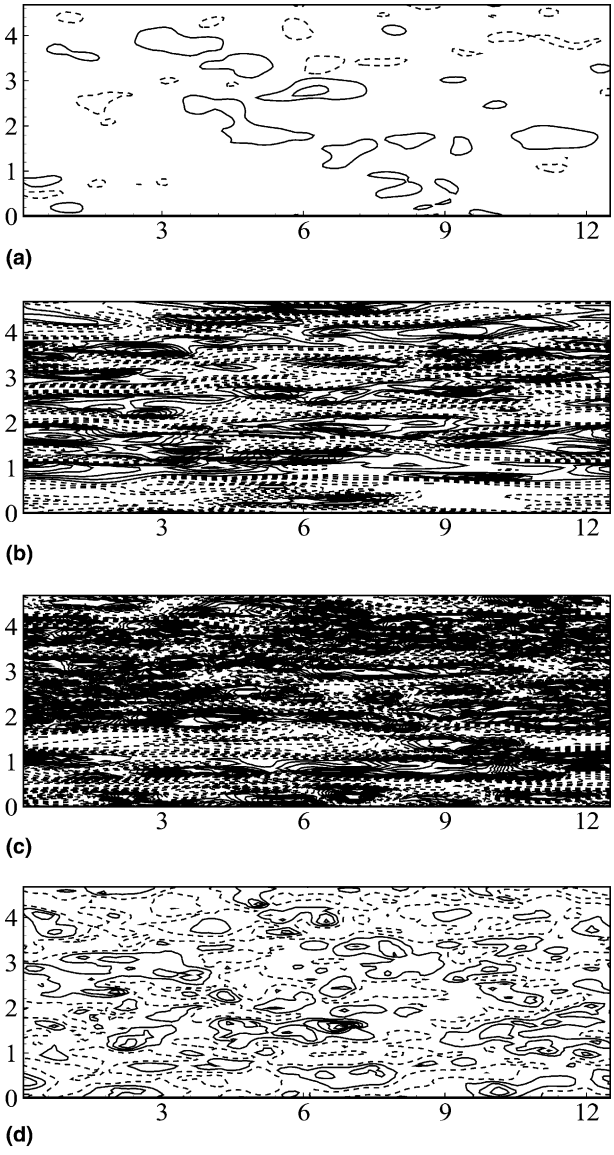

Fig. 15. Contours of instantaneous resolved streamwise velocity fluctuation in the (x, y) plane at $z^+ = 6.5$ for $\omega_P = 1$: (a) $t/t_P = 0/4$; (b) 1/4; (c) 2/4; (d) 3/4. Here, solid lines represent positive values and dashed lines negative values. Increment of the contours is 1.

experimental observations [1–3] and can be explained by considering the surface flow kinematics. Based on the velocity and vorticity fields near the free surface, these events and the activity of the turbulence near the free surface were investigated in our previous study [24]. Thus, the flow patterns with absent and healthy streaky structures given in Fig. 16 for different phases are consistent with those near the bottom wall in Fig. 17 and agree with the time evolution of the phase-averaged streamwise turbulence intensity near the free surface in Fig. 6a. Meanwhile, the time development

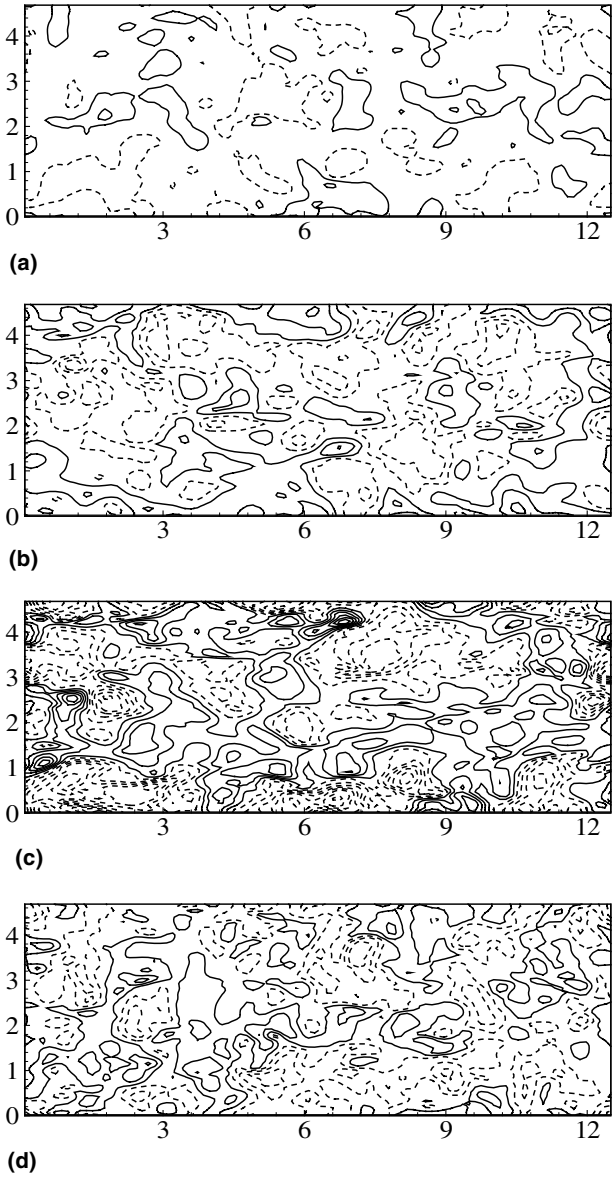

Fig. 16. Contours of instantaneous resolved streamwise velocity fluctuation field in the (x,y) plane at $z^+ = 173.5$ for $\omega_P = 1$: (a) $t/t_P = 0/4$; (b) 1/4; (c) 2/4; (d) 3/4. Increment of the contours is 1.

of the structures in Fig. 17 is also qualitatively consistent with the corresponding turbulence feature entering the free surface-influenced region, as listed in Table 2.

Based on experimental observation [1–4], the most surface renewal events are due to bursting processes near the solid boundary and are closely correlated with boundary layer bursts. Here, the patterns of instantaneous streamwise velocity fluctuation in the (x,z) plane for $\omega_P = 1$ are shown in Fig. 17. The well-known high-speed streaks (dense solid lines) are clearly illustrated. Moin and

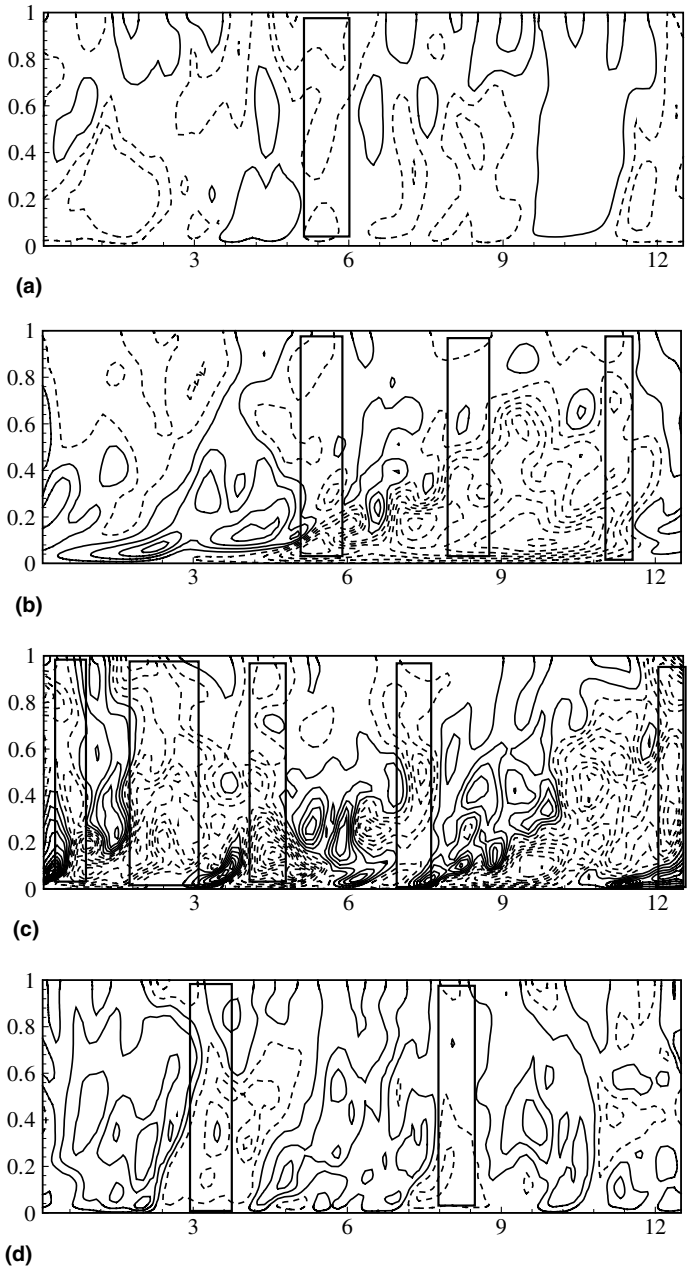

Fig. 17. Contours of instantaneous resolved streamwise velocity fluctuation in the (x, y, z) plane for $\omega_P = 1$: (a) $t/t_P = 0/4$; (b) 1/4; (c) 2/4; (d) 3/4. Increment of the contours is 1. The regions marked by the squares correspond to the ejection processes with the contour plots extending from the bottom wall to the free surface with negative streamwise velocity fluctuation [43].

Kim [43] postulated that the wall layer may be viewed as a bed of low-speed fluid that is constantly subjected to the arrival of energetic eddies from the outer layers. These energetic eddies

form the high-speed streaks in the wall region. Thus, as observed in Fig. 17, the bursting processes near the bottom wall are ejected toward the free surface, corresponding to the contour plots

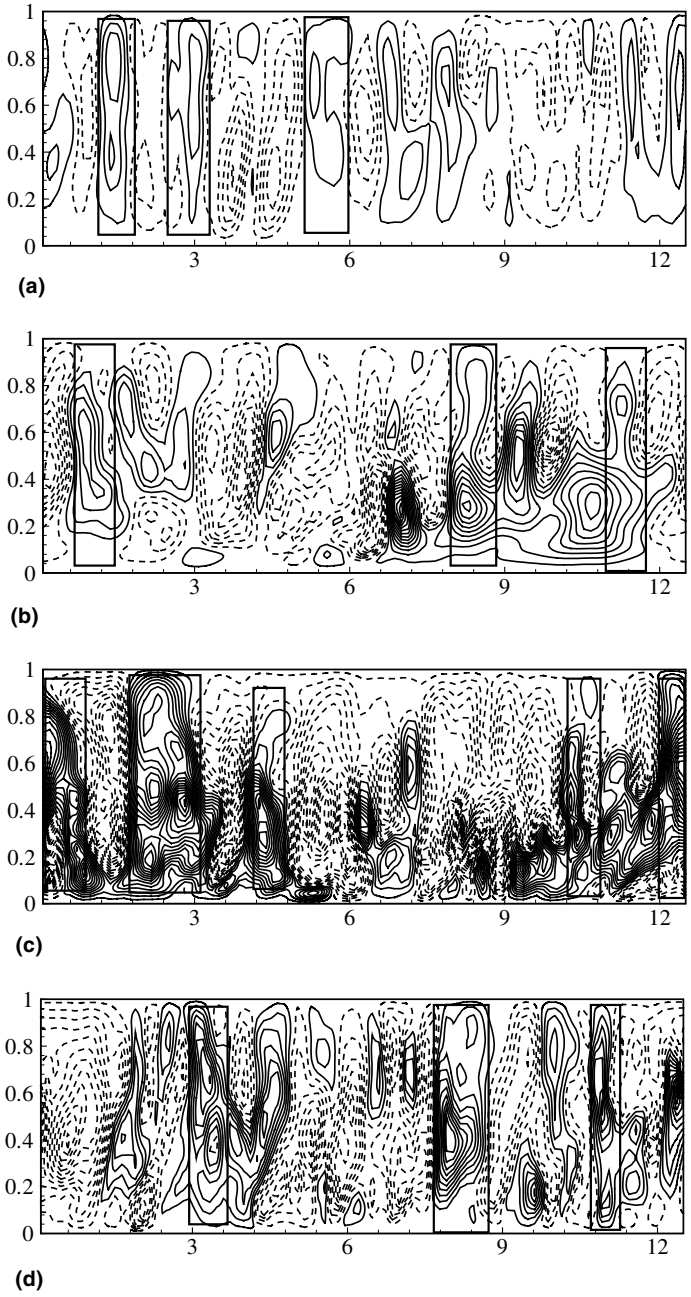

Fig. 18. Contours of instantaneous resolved vertical velocity fluctuation in the (x, z) plane for $\omega_P = 1$: (a) $t/t_P = 0/4$; (b) 1/4; (c) 2/4; (d) 3/4. Increment of the contours is 0.25. The regions marked by the squares correspond to the "splatting events" with positive vertical velocity fluctuation [2,24].

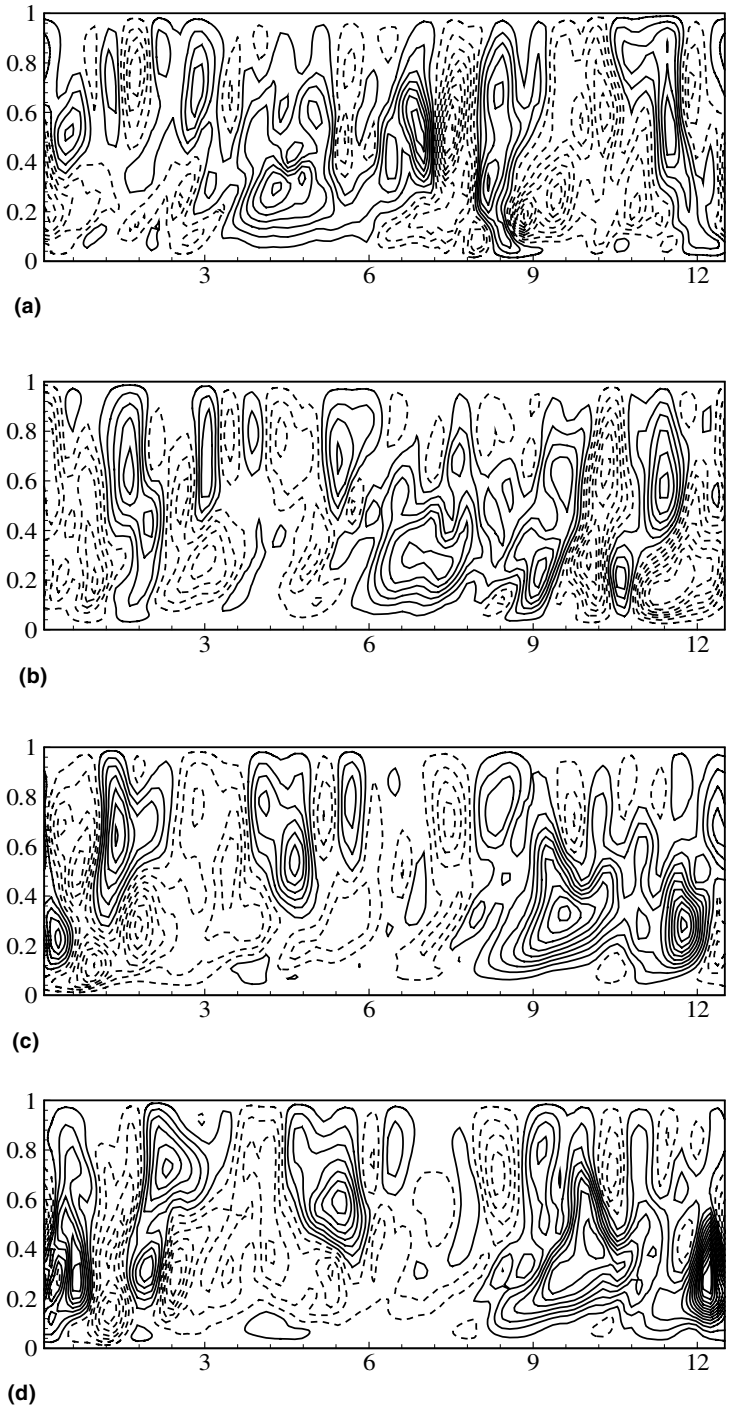

Fig. 19. Contours of instantaneous resolved vertical velocity fluctuation in the (x,z) plane for $\omega_P = 14$: (a) $t/t_P = 0/4$; (b) 1/4; (c) 2/4; (d) 3/4. Increment of the contours is 0.25.

extending from the bottom wall to the free surface with negative streamwise velocity fluctuation [43] and marked by the squares in Fig. 17. During the decelerating phase, e.g., $t/t_P = 2/4$ (Fig. 17c), stronger ejection events appear frequently compared to those during the accelerating phase, e.g., $t/t_P = 0/4$ (Fig. 17a). Meanwhile, it is interesting to find that the streak structures are swept downward along the streamwise direction during the acceleration phases and recovered around the end of the deceleration period.

It is known that eruption process of fluid from the bottom wall region usually retains their coherence in the sequence of convecting toward the free surface [5–7]. The upward process eventually reaches the free surface as so-called "splatting events" and is closely related to the vertical velocity fluctuation. To understand these events near the free surface and to indicate the activity of the turbulence near the free surface, corresponding to Fig. 17, the instantaneous vertical velocity fluctuation fields are exhibited in Fig. 18. The structures with the closed contours with an alternated approximately arrangement of positive and negative values spread over the core region of the channel. These organized streaks of the vertical velocity fluctuation, as marked by squares in Fig. 18 for the "splatting events" with positive vertical velocity fluctuation [2,24], are connected with bursting processes. It is reasonably observed that the vertical velocity fluctuation with healthy streaky structures is stronger at the decelerating phase $t/t_P = 2/4$ (Fig. 18c) compared to that at the accelerating phase $t/t_P = 0/4$ (Fig. 18a). This behavior is related to different characteristics of the intercomponent energy transfer and the turbulence production during the acceleration and deceleration phase.

To exhibit the effect of driving frequency on turbulent flow structures, Fig. 19 shows the instantaneous vertical velocity fluctuation fields for $\omega_P = 14$. Although the flow structures are obviously different for several phases, as discussed early and shown in Fig. 8, statistical quantities still have the similar characteristics for different phases.

5. Concluding remarks

Large eddy simulation of pulsating turbulent open channel flow is performed to investigate the behaviors of the pulsating turbulent flow. The decisive validation of the present approach has been achieved by comparing our calculated results with some available computational and experimental results. Based on our calculated results, it is found that the depth of the surface-influenced layer increases and the turbulent Stokes length near the bottom wall decreases with the increase of the driving frequency. Turbulence intensities in the surface-influenced region reveal that turbulent flow has a strong anisotropy near the shear free boundary, in particular during the decelerating phase. Analyses of the resolved turbulent kinetic energy and Reynolds stresses budgets represent that the turbulence energy in the vertical direction is transferred into the free surface parallel directions through the pressure-strain effect. The completely different features of turbulence structures, in terms of viscous sublayer and the semi-logarithmic profile, between the accelerating and decelerating phases can be identified. The time development of the flow structures is closely related to the characteristics of the intercomponent energy transfer and the turbulence production during the acceleration and deceleration phase. The flow structures clearly exhibit that the bursting processes near the bottom wall are ejected toward the surface and the most surface renewal events are correlated with the bursting processes. These processes during the decelerating period

are strengthened, compared to those during the accelerating period based on the time development of flow structures.

Acknowledgements

This work was supported by the National Natural Science Foundation of China (No. 90405007, 10125210, 10302028), the China NKBRSF Project (No. 2001CB409600), the Programme of the Hundred-Talent of the Chinese Academy of Sciences, and Specialized Research Fund for the Doctoral Program of Higher Education (No. 20020358013).

Appendix A. Equations for statistical quantities

The equation for the resolved turbulent kinetic energy (TKE) $k = \langle u_i' u_i' \rangle / 2$ can be written as (non-dimensionalized as above)

$$\frac{\partial k}{\partial t} = \mathrm{PR} + \mathrm{DS} + \mathrm{TD} + \mathrm{VD} + \mathrm{PD}, \tag{A.1}$$

where the terms on the right-hand side are

$$\mathrm{PR} = -\langle u_1' u_3' \rangle \frac{\partial \langle u_1 \rangle}{\partial x_3}, \quad \text{production rate;}$$

$$\mathrm{DS} = -\frac{1}{Re_\tau} \left\langle \frac{\partial u_i'}{\partial x_k} \frac{\partial u_i'}{\partial x_k} \right\rangle, \quad \text{viscous dissipation;}$$

$$\mathrm{TD} = -\frac{1}{2} \frac{\partial \langle u_i' u_i' u_3' \rangle}{\partial x_3}, \quad \text{turbulent diffusion;}$$

$$\mathrm{VD} = \frac{1}{Re_\tau} \frac{\partial^2 k}{\partial x_3 \partial x_3}, \quad \text{viscous diffusion;}$$

$$\mathrm{PD} = -\frac{\partial \langle p' u_3' \rangle}{\partial x_3}, \quad \text{pressure velocity diffusion.}$$

The transport equation for the resolved spanwise Reynolds stress $\langle u_2' u_2' \rangle$ (or $\langle v' v' \rangle$) can be obtained

$$\frac{\partial}{\partial t} \langle u_2' u_2' \rangle = \mathrm{PS} + \mathrm{DS} + \mathrm{TD} + \mathrm{VD}, \tag{A.2}$$

where the various terms are

$$\mathrm{PS} = 2 \left\langle p' \frac{\partial u_2'}{\partial x_2} \right\rangle, \quad \text{pressure-strain correlation;}$$

$$\mathrm{DS} = -\frac{2}{Re_\tau}\left\langle \frac{\partial u_2'}{\partial x_k}\frac{\partial u_2'}{\partial x_k}\right\rangle, \quad \text{viscous dissipation;}$$

$$\mathrm{TD} = -\frac{\partial\langle u_2'^2 u_3'\rangle}{\partial x_3}, \quad \text{turbulent diffusion;}$$

$$\mathrm{VD} = \frac{1}{Re_\tau}\frac{\partial^2\langle u_2'^2\rangle}{\partial x_3\,\partial x_3}, \quad \text{viscous diffusion.}$$

The transport equation for the resolved vertical Reynolds stress $\langle u_3' u_3'\rangle$ (or $\langle w'w'\rangle$) can be obtained

$$\frac{\partial}{\partial t}\langle u_3' u_3'\rangle = \mathrm{PD} + \mathrm{PS} + \mathrm{DS} + \mathrm{TD} + \mathrm{VD}, \tag{A.3}$$

where the various terms are

$$\mathrm{PD} = -2\frac{\partial\langle p' u_3'\rangle}{\partial x_3}, \quad \text{pressure velocity diffusion;}$$

$$\mathrm{PS} = 2\left\langle p'\frac{\partial u_3'}{\partial x_3}\right\rangle, \quad \text{pressure-strain correlation;}$$

$$\mathrm{DS} = -\frac{2}{Re_\tau}\left\langle \frac{\partial u_3'}{\partial x_k}\frac{\partial u_3'}{\partial x_k}\right\rangle, \quad \text{viscous dissipation;}$$

$$\mathrm{TD} = -\frac{\partial\langle u_3'^3\rangle}{\partial x_3}, \quad \text{turbulent diffusion;}$$

$$\mathrm{VD} = \frac{1}{Re_\tau}\frac{\partial^2\langle u_3'^2\rangle}{\partial x_3\,\partial x_3}, \quad \text{viscous diffusion.}$$

References

[1] Nakagawa H, Nezu I. Structure of space–time correlations of bursting phenomena in open-channel flow. J Fluid Mech 1981;104:1–43.
[2] Komori S, Murakami Y, Ueda H. The relationship between surface-renewal and bursting motions in an open-channel. J Fluid Mech 1989;203:103–23.
[3] Komori S, Nagaosa R, Muramami Y. Turbulence structure and mass transfer across a sheared air–water interface in wind driven turbulence. J Fluid Mech 1993;249:161–83.
[4] Kumar S, Gupta R, Banerjee S. An experimental investigation of the characteristics of free-surface turbulence in channel flow. Phys Fluids 1998;10:437–56.
[5] Rashidi M, Banerjee S. Turbulence structure in free surface flows. Phys Fluids 1988;31:2491–503.
[6] Rashidi M, Hetstroni G, Banerjee S. Mechanisms of heat and mass transport at gas–liquid interfaces. Int J Heat Mass Transfer 1991;34:1799–805.
[7] Rashidi M. Burst-interface interactions in free surface turbulent flows. Phys Fluids 1997;9:3485–501.

[8] Komori S, Nagaosa R, Murakami Y, Chiba S, Ishii K, Kuwahara K. Direct numerical simulation of three-dimensional open-channel flow with zero-shear gas–liquid interface. Phys Fluids 1993;5:115–25.
[9] Pan Y, Banerjee S. A numerical study of free-surface turbulence in channel flow. Phys Fluids 1995;7:1649–64.
[10] Lombardi P, De Angelis V, Banerjee S. Direct numerical simulation of near-interface turbulence in coupled gas–liquid flow. Phys Fluids 1996;8:1643–65.
[11] Tsai W-T. A numerical study of the evolution and structure of a turbulent shear layer under a free surface. J Fluid Mech 1998;354:239–76.
[12] Nagaosa R. Direct numerical simulation of vortex structures and turbulent scalar transfer across a free surface in a fully developed turbulence. Phys Fluids 1999;11:1581–95.
[13] Handler RA, Saylor JR, Leighton RI, Rovelstad AL. Transport of a passive scalar at a shear-free boundary in fully developed turbulent open channel flow. Phys Fluids 1999;11:2607–25.
[14] Germano M, Piomelli U, Moin P, Cabot W. A dynamic subgrid-scale eddy viscosity model. Phys Fluids 1991;3:1760–5.
[15] Smagorinsky J. General circulation experiments with the primitive equations. I. The basic experiment. Mon Weather Rev 1963;91:99–165.
[16] Wang W-P, Pletcher RH. On the large eddy simulation of a turbulent channel flow with significant heat transfer. Phys Fluids 1996;8:3354–66.
[17] Zang Y, Street RL, Koseff JR. A dynamic mixed subgrid-scale model and its application to turbulent recirculating flows. Phys Fluids 1993;5:3186–96.
[18] Liu NY, Lu XY, Zhuang LX. A new dynamic subgrid-scale model for the large eddy simulation of stratified turbulent flows. Sci China A 2000;43:391–9.
[19] Zhong FQ, Liu NS, Lu XY, Zhuang LX. An improved dynamic subgrid-scale model for the large eddy simulation of stratified channel flow. Sci China A 2002;45:888–99.
[20] Dong YH, Lu XY, Zhuang LX. An investigation of Prandtl number effects on turbulent heat transfer in channel flows by large eddy simulation. Acta Mech 2002;159:39–51.
[21] Dong YH, Lu XY, Zhuang LX. Large eddy simulation of turbulent channel flow with mass transfer at high-Schmidt numbers. Int J Heat Mass Transfer 2003;46:1529–39.
[22] Salvetti MV, Zang Y, Street RL, Banerjee S. Large-eddy simulation of free-surface decaying turbulence with dynamic subgrid-scale models. Phys Fluids 1997;9:2405–19.
[23] Calmet I, Magnaudet J. Statistical structure of high-Reynolds-number turbulence close to the free surface of an open-channel flow. J Fluid Mech 2003;474:355–78.
[24] Wang L, Dong YH, Lu XY. An investigation of turbulent open channel flow with heat transfer by large eddy simulation. Comput Fluid 2005;34:23–47.
[25] Lu XY, Dalton C, Zhang J. Application of large eddy simulation to an oscillating flow past a circular cylinder. ASME J Fluid Eng 1997;119:519–25.
[26] Hsu CT, Lu XY, Kwan MK. LES and RANS studies of oscillating flows over a flat plate. ASCE J Eng Mech 2000;126:186–93.
[27] Scotti A, Piomelli U. Numerical simulation of pulsating turbulent channel flow. Phys Fluids 2001;13:1367–84.
[28] Wang L, Lu XY. An investigation of turbulent oscillatory heat transfer in channel flows by large eddy simulation. Int J Heat Mass Transfer 2004;47:2161–72.
[29] Costamagna P, Vittori G, Blondeaux P. Coherent structures in oscillatory boundary layers. J Fluid Mech 2003;474:1–33.
[30] Vittori G, Verzicco R. Direct simulation of transition in an oscillatory boundary layer. J Fluid Mech 1998;371:207–32.
[31] Akhavan R, Kamm RD, Shapiro AH. An investigation of transition to turbulence in bounded oscillatory Stokes flows. Part 2. Numerical simulations. J Fluid Mech 1991;225:423–44.
[32] Spalart PR, Baldwin BS. Direct simulation of a turbulent oscillating boundary layer. In: Andre JC, Cousteix J, Durst F, Launder B, Schmidt F, Whitelaw J, editors. Turbulent shear flows, vol. 6. Springer; 1988.
[33] Verzicco R, Orlandi P. A finite-difference scheme for three-dimensional incompressible flows in cylindrical coordinates. J Comput Phys 1996;123:402–14.
[34] Sarghini F, Piomelli U, Balaras E. Scale-similar models for large-eddy simulations. Phys Fluids 1999;11:1596–607.

[35] Dong YH, Lu XY. Large eddy simulation of a thermally stratified turbulent channel flow with temperature oscillation on the wall. Int J Heat Mass Transfer 2004;47:2109–22.
[36] Tardu S, Binder G, Blackwelder RF. Turbulent channel flow with large-amplitude velocity oscillations. J Fluid Mech 1994;267:109–51.
[37] Hino M, Kashiwayanagi M, Nakayama A, Hara T. Experiments on the turbulence statistics and the structure of a reciprocating oscillatory flow. J Fluid Mech 1983;131:363–400.
[38] Tu SW, Ramaprian BR. Fully developed periodic turbulent pipe flow. Part 1. Main experimental results and comparison with predictions. J Fluid Mech 1983;137:31.
[39] Binder G, Tardu S, Vezin P. Cyclic modulation of Reynolds stresses and length scales in pulsed turbulent channel flow. Proc R Soc London, Ser A 1995;451:121–30.
[40] Perot B, Moin P. Shear-free boundary layers: 1. Physical insights into near wall turbulence. J Fluid Mech 1995;295:199–227.
[41] Swean TF, Leighton RI, Handler RA, Swearingen JD. Turbulence modeling near the free surface in an open channel flow. AIAA Paper 91-0613; 1991.
[42] Sarpkaya T. Coherent structures in oscillatory boundary layers. J Fluid Mech 1993;253:105–40.
[43] Moin P, Kim J. Numerical investigation of turbulent channel flow. J Fluid Mech 1982;118:341–77.